



## Research Paper

## Isothermic adsorption of morin onto the reducible mesoporous manganese oxide materials surface



Ali K. Ilunga, Itumeleng R. Legodi, Simbongile Gumbi, Reinout Meijboom\*

Department of Chemistry, University of Johannesburg, PO Box 524, Auckland Park 2006, Johannesburg, South Africa

## ARTICLE INFO

## Keywords:

Manganese oxide  
Mesoporous materials  
Reducibility  
Physicochemical adsorption  
Oxidation process

## ABSTRACT

A series of mesoporous manganese oxide materials were synthesized following the inverse micelle sol-gel method and categorized by the heat treatment. The tunable features and crystallinity of the mesoporous materials were analyzed by BET and XRD analyses. The HR-TEM and TRP analyses were conducted to analyze the meso-ordered structure and reducibility of the mesoporous manganese oxide materials. The catalytic activity of the mesoporous materials was investigated in aerobic oxidation of morin as a model reaction. The experimental data were interpreted according to the Mars-van Krevelen and Langmuir-Hinshelwood approach. The heat treatment influenced the crystallite size and the activity of the mesoporous manganese oxide materials. The activity of the lattice oxygen was a critical factor in the aerobic process.  $MnO_2$ –350 °C exhibited the largest lattice oxygen activity ( $(64.3 \pm 5.6) \times kJ mol^{-1} m^{-2}$ ).

## 1. Introduction

Since the first report on mesoporous materials by the Mobil Oil company, a range of mesoporous materials was synthesized and used in numerous scientific fields such as catalysis and medicine [1]. Applied as active particles support or catalyst, the large surface area and thermal stability of the mesoporous materials is the main reason which justified its numerous applications [2]. Mesoporous transition metal oxide materials are used in energy storage, drug delivery, and catalysis [3–5].

Yang et al. reviewed functionalized mesoporous silica in biomedical applications for drug delivery [6]. Mesoporous manganese oxide materials synthesized by co-electrodeposition were reported for electrochemical energy storage [7].

The tunable features of mesoporous materials such as porosity or surface area are the important factor justifying its catalytic application [8]. The largest surface area and porosity of the mesoporous materials facilitated the interfacial interaction with the reactants. The interfacial interaction is defined as a physicochemical adsorption of the substrate on the solid surface (catalyst) resulting in the improvement of the catalytic process [9]. Mesoporous manganese oxide was reported as a catalyst in the double oxidation of 1-decanol to 1-decanoic acid [10]. Using metal oxides as a catalyst for an oxidation process, the lattice oxygen can play a crucial role as the oxidizing agent through an interfacial interaction with the substrates. The lattice oxygen in vanadium oxide has been reported as an oxidant in the aerobic oxidation of methanethiol to formaldehyde [11].

The hydrolytic condensation process is a crucial step governing the synthesis of mesoporous materials following a sol-gel approach [12,13]. However, the use of water during the sol-gel synthesis weakens meso-frameworks due to the thermal limitation of hydrogen bond [14,15]. Investigations are ongoing to avoid the use of water as a medium during the course of mesoporous material synthesis. Poyraz et al. developed an inverse micelle sol-gel method to synthesize the mesoporous metal oxide materials in an alcoholic medium [16]. The resulting porosity of the mesoporous materials was attributed to a thermal decomposition of nitrous oxide [17].

The discharge of dye compounds into wastewater from textile industry is a major environmental problem to the ecosystem [18]. The degradation of dye compounds prior to being released into wastewater is one of best responses to the wastewater toxication. Among the techniques performed in wastewater contamination prevention, oxidation is conducted as a post and pre-treatment method [19]. A flavonol compound such as morin (2-(2,4-dihydroxyphenyl)-3,5,7-trihydroxy-4H-chromen-4-one) can be used as a model compound in the catalytic activity investigation of the catalyst [20]. Morin undergoes an oxidation easily and the ortho-position of the hydroxyl group in the morin structure facilitates the kinetic data interpretation by preventing its dimerization [21,22]. Morin oxidation results in two main products which are 2,4-dihydroxybenzoic acid and 2,4,6-trihydroxybenzoic acid [21,22]. The oxidation pathway of morin is not precisely known compared to the quercetin compound oxidation [23,24].

The interfacial interaction with the substrate can be evaluated

\* Corresponding author.

E-mail address: [rmeijboom@uj.ac.za](mailto:rmeijboom@uj.ac.za) (R. Meijboom).

through an adsorption system at a given temperature and pH [9]. The substrate transfer from the liquid or gas phase to the catalyst surface resulted in physicochemical bond formation. Several mathematical approaches have been developed to interpret the experimental data of the isothermal adsorption process [25]. The Langmuir-Hinshelwood and Mars-van Krevelen approaches are often applied in studying the interface interaction of catalyst and substrates [26]. Polzer et al. studied the liquid phase transfer of morin (substrate) to the manganese oxide nanoparticle surface as a catalyst using the Langmuir-Hinshelwood approach [22].

In the current investigation, mesoporous manganese oxide materials were synthesized using the inverse micelle sol-gel method and evaluated as catalysts in the environmental cleaning process. The aerobic oxidation of morin was conducted as a model reaction. The mesoporous manganese oxide materials were subdivided based on the heat treatment (150 °C, 250 °C, 350 °C, 450 °C, and 550 °C) and each of them was used as a catalyst. The Mars-van Krevelen and Langmuir-Hinshelwood adsorption isotherm approaches will be applied to interpret the kinetic data of morin oxidation. A comparative conclusion between the crystallinity and catalytic activity of the mesoporous manganese oxide materials will be drawn.

## 2. Experimental section

For the synthesis of mesoporous manganese oxide materials, the sol-gel inverse micelle approach developed by Biswas et al. was adopted [10]. Pluronic® P-123 ( $\geq 98.0\%$ , Sigma-Aldrich) was used as a nanoreactor to control the oxo-cluster aggregation. Exactly, 1.97 g ( $3.4 \times 10^{-4}$  mol) of P-123 (surfactant gel) was dissolved in an alcoholic acidified solution of  $1.52 \times 10^{-3}$  L (0.032 mol) of nitric acid ( $\geq 55.0\%$ , Rochelle chemical) and  $17.20 \times 10^{-3}$  L (0.188 mol) of 1-butanol ( $\geq 99.5\%$ , Rochelle chemical). The amount of 5.13 g (0.02 mol) of manganese(II) nitrate tetrahydrate ( $\geq 99.0\%$ , Sigma-Aldrich) was added and stirred to a complete dissolution. The resulting gel was heated in an oven for four hours at 120 °C. The resulting brown powder was washed three times with an excess of ethanol ( $\geq 95.0\%$ , Rochelle chemical) to remove the surfactant. The brown powder was centrifuged and dried in an oven overnight at 50 °C. The brown powder was subjected to the heating cycle process which will improve the tunable features and crystallinity of the materials. The heating cycle was subdivided into five steps. Prior to performing the subsequent heat step, the material was cooled and the required amount saved. The five heating steps with the corresponding times are 150 °C (12 h), 250 °C (4 h), 350 °C (3 h), 450 °C (2 h) and 550 °C (1 h).

The nitrogen gas isothermic adsorption and desorption on mesoporous materials were analyzed at a maximum relative pressure of 1P/P<sub>0</sub> using a Micrometrics Tristar to determine the tunable features of manganese oxide materials. The amount ranging 0.1–0.3 g of manganese oxide materials were used to perform Brunauer, Emmett and Teller analysis (BET) [27]. A Rigaku MiniFlex 600 was used to perform the X-ray diffraction analysis (XRD) of manganese oxide materials. The diffraction analysis was performed at two angles, a low (0.5–10°) and wide (10–70°) angle. The crystallite size of the manganese oxide materials was calculated using the Scherrer equation [28].

The temperature programmed reduction analysis (TPR) was conducted using a Micromeritics AutoChem II to analyze the manganese oxide materials reducibility. Ten percentage of hydrogen gas contained in the H<sub>2</sub>-He gas mixture was used to reduce the metal oxide materials at flow rate of  $10^{\circ}\text{C min}^{-1}$ . At a temperature range of 50–700 °C, a mass ranging 0.03–0.04 g of the manganese oxide materials was used to conduct the TPR analysis. Micrographs of the mesoporous manganese oxide materials were captured using a JOEL JEM-2100F electron microscope. Using a microcentrifuge tube, a small amount of manganese oxide material was mixed with an excess of ethanol. The slurry was sonicated to improve the dispersion for 30 min. The copper grid was dipped into the solution and dried at room temperature prior to

performing the high-resolution transmission electron microscopy analysis (HR-TEM).

In a two-neck round-bottom flask, a total volume of  $20 \times 10^{-3}$  L of deionized water (obtained from an in-house Milli-Q system) was used to perform the catalytic investigation. Exactly,  $60 \times 10^{-6}$  M of morin prepared in  $1 \times 10^{-3}$  M of carbonate buffer was used to perform the process. The carbonate buffer was prepared using an equivalent molar ratio of sodium carbonate ( $\geq 98.0\%$ , Merck Laboratories) and sodium bicarbonate ( $\geq 99.5\%$ , Merck Laboratories), to stabilize the pH at 10. Using an air pump (HAILEA Super Silent Design Air Pump (ACO-2201)), the oxygen gas continuously flowed at the rate of  $21.7 \times 10^{-3}$  L s<sup>-1</sup> into the morin solution. The desired amount of mesoporous manganese oxide materials was added last to start the catalytic process. UV-vis spectrophotometry (Shimadzu UV-1800 spectrophotometer) was used to monitor the light absorption decreasing at  $\lambda = 410$  nm which corresponds to the maximum absorbance peak of morin.

The catalyst effect investigation was conducted at a given concentration of morin ( $60 \times 10^{-6}$  M) under continuously pumped air at constant flow rate of  $21.7 \times 10^{-3}$  L s<sup>-1</sup>. The use of a small amount of the catalysts during the catalyst effect study was achieved by dispersing  $10 \times 10^{-3}$  g of the mesoporous manganese oxide materials in  $10 \times 10^{-3}$  L of deionized water. A varied amount of the catalyst was used for the investigation and the slurry was filtered prior to performing the light absorption spectrophotometry. The catalyst slurry was kept stirring for two days to investigate the water stability of the catalyst. The water stability of the catalyst was confirmed by ICP-MS analysis of the supernatant using Shimadzu ICP-MS 2030.

The isothermal adsorption process was thermally evaluated to determine the kinetic and thermodynamic parameters. Exactly, three temperatures were considered 25 °C, 35 °C, and 45 °C for the temperature effect investigation. Only the physicochemical adsorption of morin onto the catalysts was investigated. The isothermal adsorption of the oxygen gas was not evaluated due to the fact that a continuing and constant flow rate ( $21.7 \times 10^{-3}$  L s<sup>-1</sup>) of oxygen gas was applied to during the course of the full investigation. The isothermal adsorption of morin onto the mesoporous materials was investigated using a concentration ranging ( $(30\text{--}100) \times 10^{-6}$  M) of morin. OriginPro 8.5, data analysis and graphing software, was used to analyze and fit the experimental data according to the Mars-van Krevelen and Langmuir-Hinshelwood models.

## 3. Results

The heat treatment at 120 °C of a manganese nitrate gel resulted in a brown powder which was subjected to the heating cycle process. The heating cycle shifted the color of mesoporous manganese oxide materials to black. The heating cycle results in a major modification of the intrinsic properties of mesoporous manganese oxide materials such as tunable features, crystallinity, and reducibility. The first heating cycle process conducted at 150 °C for 12 h consisted of the complete removal of the nitric and carbonyl species [16]. The tunable features analyzed through BET analysis are shown in Fig. 1(a–b), the surface area and pore volume, respectively. The surface area of the mesoporous manganese oxide materials evolved inversely to the heat treatment temperature. The BJH desorption analysis resulted in a quite large pore size distribution of the mesoporous manganese oxide materials. Table 1 shows the numeric values of tunable features (surface area, pore size, and pore volume) versus the heat treatment of mesoporous manganese oxide materials.

The XRD analysis conducted at low and wide angles indicate a number of reflecting angles. The X-ray diffraction analysis is depicted in Fig. 2(a–b), low and wide angles, respectively. The resulting diffraction peaks were matched to the software database. MnO<sub>2</sub>–150 °C matched to MnO crystallinity corresponding to 96-441-7967 JCS number. The matching of MnO<sub>2</sub>–250 °C resulted in 60% of MnO<sub>2</sub> and 40% of MnO

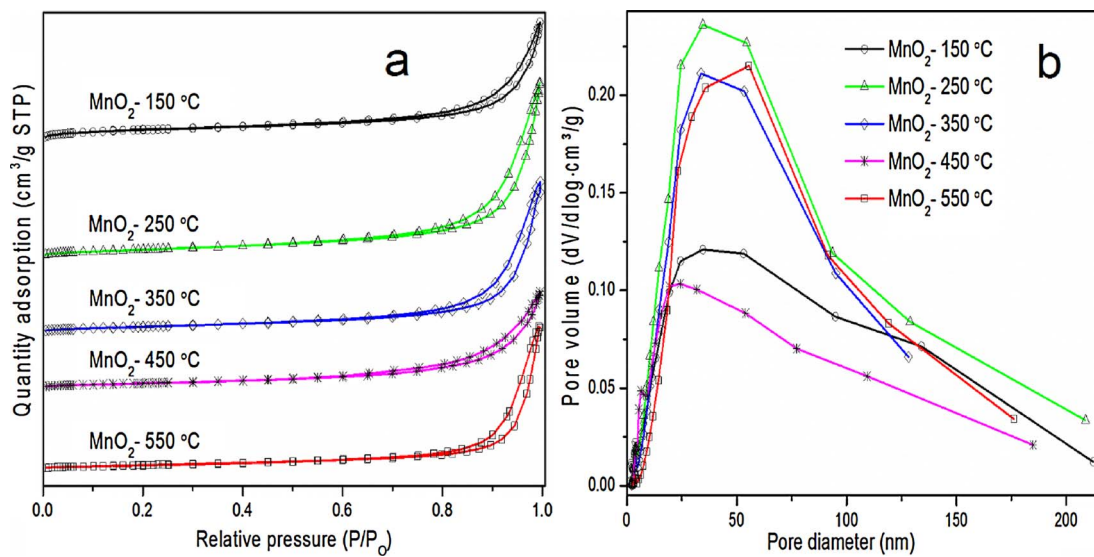


Fig. 1. (a) and (b) described the isotherm plots of the nitrogen gas adsorption on manganese oxide materials.

Table 1  
BET and XRD parameters obtained for each mesoporous manganese oxide materials.

MTMO	Heat treatment (°C)	Surface area (m² g⁻¹)	Pore size (nm)	Pore volume (cm³ g⁻¹)	Crystallite size (nm)
MnO <sub>2</sub>	150	31.56	15.98	0.13	8.12
	250	34.06	23.11	0.20	9.09
	350	27.10	23.88	0.16	10.34
	450	22.57	22.16	0.12	14.26
	550	21.05	31.25	0.16	15.04
	Commercial	0.06	5.42	0.012	

crystallinities related to JCSD numbers 96-900-3477 and 96-441-7967, respectively. MnO<sub>2</sub>-(350 °C–550 °C) matched to MnO<sub>2</sub> crystallinity corresponded to 96-900-3477 JCSD number. The calculated crystallite sizes of the mesoporous manganese oxide materials are given in Table 1.

The TEM micrographs of the mesoporous manganese oxide materials were captured at two different magnitudes 20 nm and 50 nm. At higher magnitude, the mesoporous materials showed various crystallite shapes whereas at lower magnification the meso-ordered frameworks

are visible. Fig. 3(a–e) shows the micrograph of the mesoporous manganese oxide materials. The TPR analysis of the mesoporous materials indicated the presence of reduction peaks. The number of reduction peaks increased along with the heat treatment temperature of the mesoporous materials. The reducing temperature of the mesoporous materials was estimated by deconvolution method using OriginPro 8.5 software. Fig. 4 shows the TPR plot of the mesoporous materials where the reducing temperature is digitally given in Table 2.

Monitoring the catalytic aerobic oxidation of morin through UV-vis spectrophotometry, three different maximum absorbance peaks were observed namely,  $\lambda$  274 nm,  $\lambda$  319 nm, and  $\lambda$  410 nm. The isosbestic points, separating each of those maximum absorbance peaks indicated the formation of new compounds and their further transformation [22]. The morin oxidation pathway is schematized in Fig. 5. The catalytic oxidation of morin can be followed at the maximum absorbance of  $\lambda$  410 nm. The UV-vis spectra depicting the aerobic oxidation of morin catalyzed by MnO<sub>2</sub>-150 °C are shown in Fig. 6a. The water stability of the catalyst investigated using MnO<sub>2</sub>-150 °C through an ICP-MS analysis resulted in leaching of 0.16 ppm of manganese species after 48 h.

The oxygen gas was continuously pumped during the catalytic process. The concentration of molecular oxygen remained

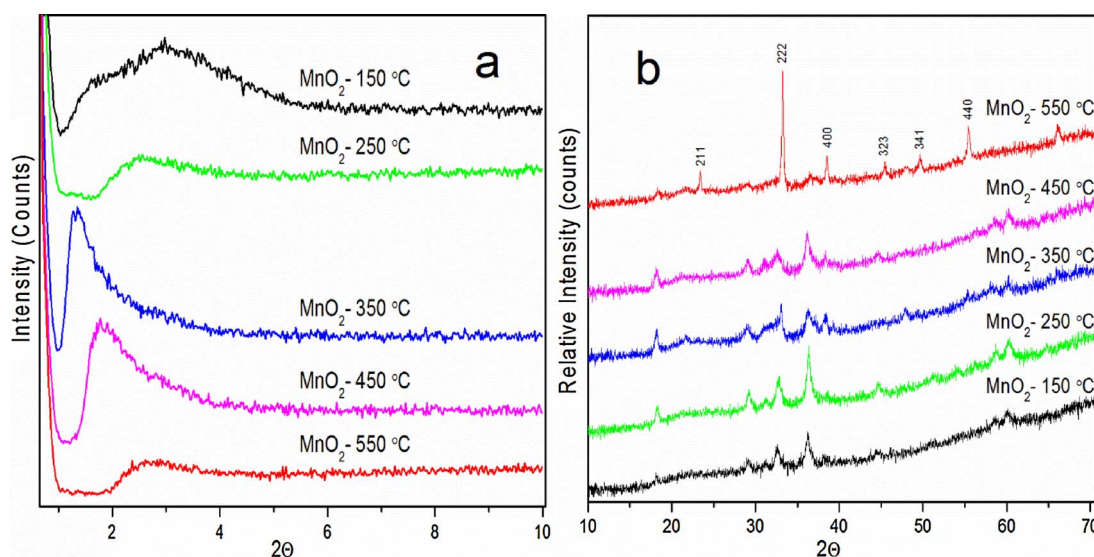


Fig. 2. The X-ray diffraction plots conducted at low (a) and wide (b) angles analysis.

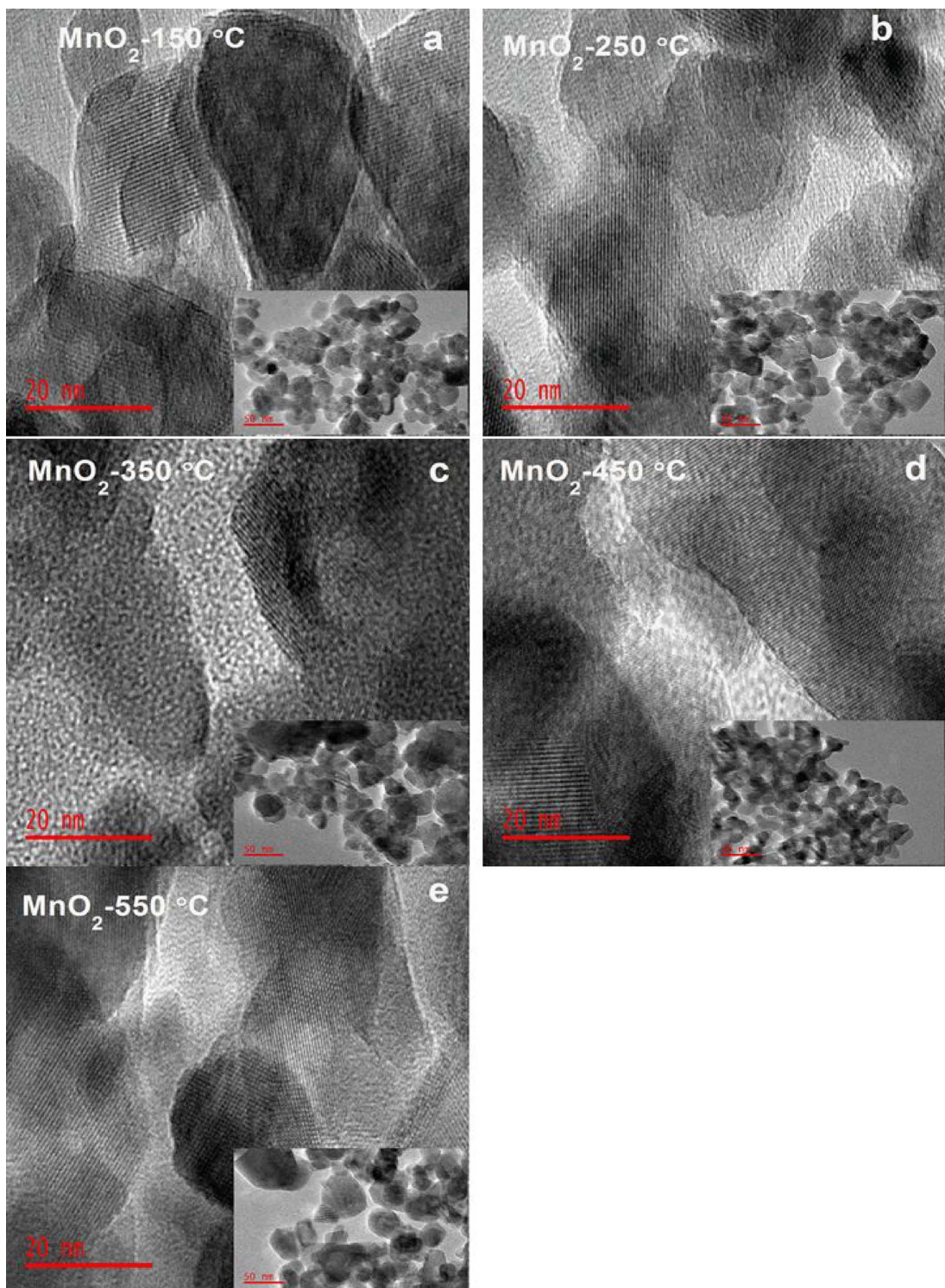


Fig. 3. Micrographs of mesoporous manganese oxide materials.

approximatively stable during the catalytic process. The catalytic process can kinetically be evaluated under *pseudo nth* order conditions [29]. The recovery of the mesoporous materials can successfully be performed by centrifugation. The kinetic evaluation can mathematically be expressed using Eq. (1a), where  $k_a$  is the kinetic coefficient, [Morin] the morin concentration,  $[O_2]$  molecular oxygen concentration, [cat] catalyst amount, and  $a$ ,  $b$ , and  $c$  are the reaction orders. Based on the negligible variation of molecular oxygen concentration and the recovery of the catalyst, the kinetic process can be investigated

under *pseudo-first* order conditions related to the concentration of morin. Eq. (1a) can be rewritten to Eq. (1b) describing the observed rate constant ( $k_{obs}$ ) of the exponential variation of morin concentration with time. The kinetic oxidation of morin is shown in Fig. 6b for different concentration of  $MnO_2-150$  °C.

$$-\frac{d[\text{Morin}]}{dt} = k_a \cdot [\text{Morin}]^a \cdot [O_2]^b \cdot [\text{Cat}]^c = k_{obs} [\text{Morin}]^a \quad (1a)$$

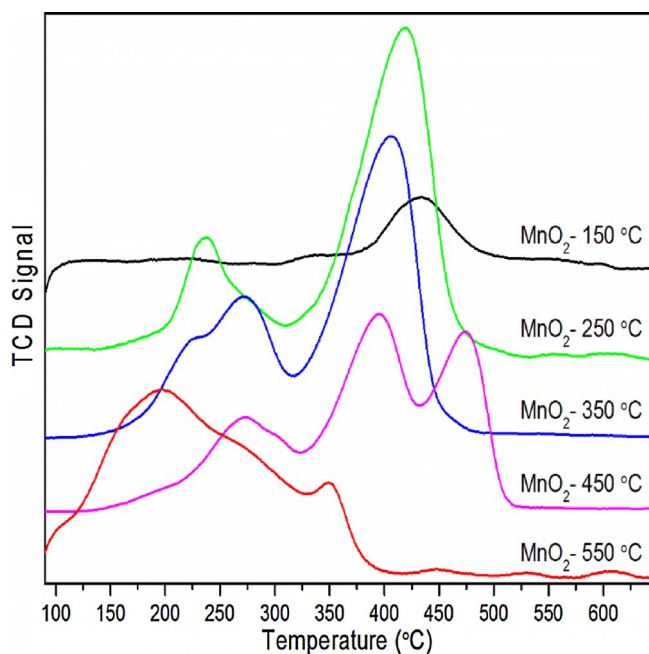


Fig. 4. The TPR plot of mesoporous manganese oxide materials performed at 50–700 °C.

Table 2  
TPR peaks of the mesoporous manganese oxide materials.

MTMO	Reduction temperature (°C)		
	First	Second	Third
MnO <sub>2</sub> -150 °C	–	341.7 ± 0.2	432.3 ± 0.3
MnO <sub>2</sub> -250 °C	–	236.3 ± 0.5	412.1 ± 0.2
MnO <sub>2</sub> -350 °C	220.9 ± 1.6	275.8 ± 0.8	413.2 ± 0.1
MnO <sub>2</sub> -450 °C	275.8 ± 0.4	393.2 ± 0.2	472.1 ± 0.1
MnO <sub>2</sub> -550 °C	184.6 ± 0.7	284.3 ± 1.2	351.9 ± 0.2

$$-\ln \frac{A_t - A_\infty}{A_0 - A_\infty} = k_{\text{obs}} \cdot t \quad (1b)$$

The catalyst effect investigation resulted in a linear increase of the observed rate constant along with the catalyst surface area. The catalyst effect of MnO<sub>2</sub>-150 °C is indicated in Fig. 6c, for the remaining mesoporous manganese oxide materials, see the supplementary information (Fig. 1S). The linear increase of the observed rate constant highlighted the catalytic activity of mesoporous materials. At a certain amount of the mesoporous manganese oxide materials, the observed rate constant indicated a horizontal development along with any evolved catalyst amount. For all the catalysts, at certain catalyst amount, the observed rate constant evolved horizontally along with the surface area. Using a

commercial manganese(IV) oxide, the catalyst effect investigation described a horizontal development during the entire process (Fig. 6d).

The catalyst amount highlighted with a green star in Fig. 6c was used to analyze the reusability of the mesoporous manganese oxide materials. Typically, the recycling run was conducted under similar conditions as the catalyst effect study (MnO<sub>2</sub>-150 °C). The catalyst recovery was conducted by centrifugation and washed with an excess volume of deionized water. The *pseudo*-first-order equation was constructed for each run performed and the plot of the observed rate constant of recycling run is depicted in Fig. 7a. The recovered catalyst from the last run was subjected to microscopy and Fig. 7b shows the micrograph of the recycled MnO<sub>2</sub>-150 °C.

The Mars-van Krevelen mechanism is often applied in oxidation process using a metal oxide as a catalyst. It can be defined as the lattice oxygen incorporation in the adsorbed substrates on the metal oxide surface. The oxidation state of the metal oxide is restored by molecular oxygen interfacially interacting with the reduced metal oxide [26]. The Langmuir-Hinshelwood mechanism defines the catalyst as a regular surface consisting of the active sites in which the substrates have to adsorb before the product formation [30]. The Langmuir-Hinshelwood mechanism has been reported in the oxidation process catalyzed by metal nanoparticles [31]. Both adsorption isotherm approaches enlighten the physicochemical adsorption of substrates onto the catalyst surface which consists of the rate determining step of the catalytic process.

The mathematical equation of both adsorption isotherm approaches, Mars-van Krevelen and Langmuir-Hinshelwood were developed in the supplementary information. Applying the interfacial interaction between the catalyst and substrates, Eq. (1a) can be rewritten by considering the surface coverage of the catalyst. The physicochemical parameters defining the interfacial interaction between the catalyst and substrate were mathematically expressed in Eqs. (2a) and (2b) based on the Mars-van Krevelen and Langmuir-Hinshelwood approach, respectively. For both adsorption isotherm approaches, three parameters were considered: the kinetic rate constant on the catalyst surface, k<sub>1</sub>, the normalized surface area of the catalyst, S, and the catalyst surface coverage, θ, to conduct the kinetic investigation [32].

$$k_{\text{obs}} = \frac{2 \cdot S \cdot k_1 \cdot k_2 \cdot k_3 \cdot [O_2]^m}{k_2 \cdot k_3 \cdot [Morin]^n + k_1 \cdot (k_2 + k_3) \cdot [O_2]^m} \quad (2a)$$

$$k_{\text{obs}} = \frac{k_1 \cdot S \cdot (K_{\text{Morin}})^n \cdot [Morin]^{n-1} \cdot (K_{O_2} \cdot [O_2])^m}{1 + (K_{\text{Morin}} \cdot [Morin])^n + (K_{O_2} \cdot [O_2])^{m-1}} \quad (2b)$$

K<sub>Morin</sub> and K<sub>O<sub>2</sub></sub> are the equilibrium constants resulting from the interfacial interaction of the catalyst with the substrates. [Morin] and [O<sub>2</sub>] are the substrate concentrations. S represents the normalized surface area of the catalyst. k<sub>1</sub> is the kinetic rate constant on the catalyst surface, where k<sub>2</sub> and k<sub>3</sub> consist of molecular oxygen dissociation and incorporation rate constants, respectively. n and m are the Sips exponents indicating the heterogeneity of the sorbent, which indicates the

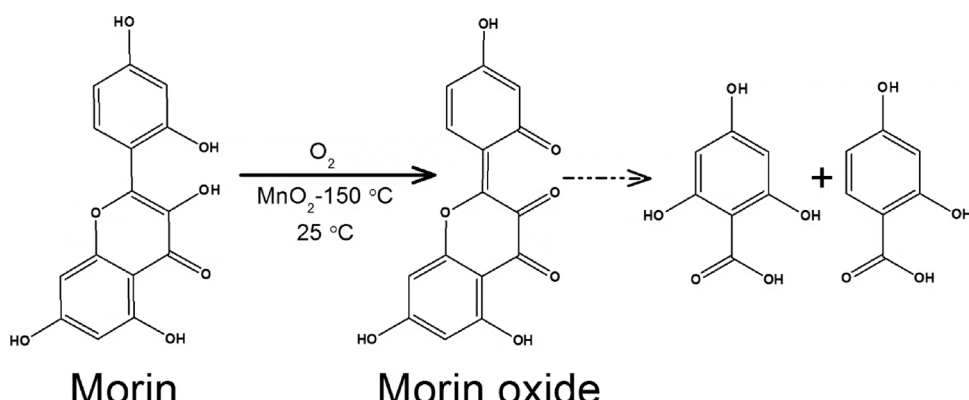
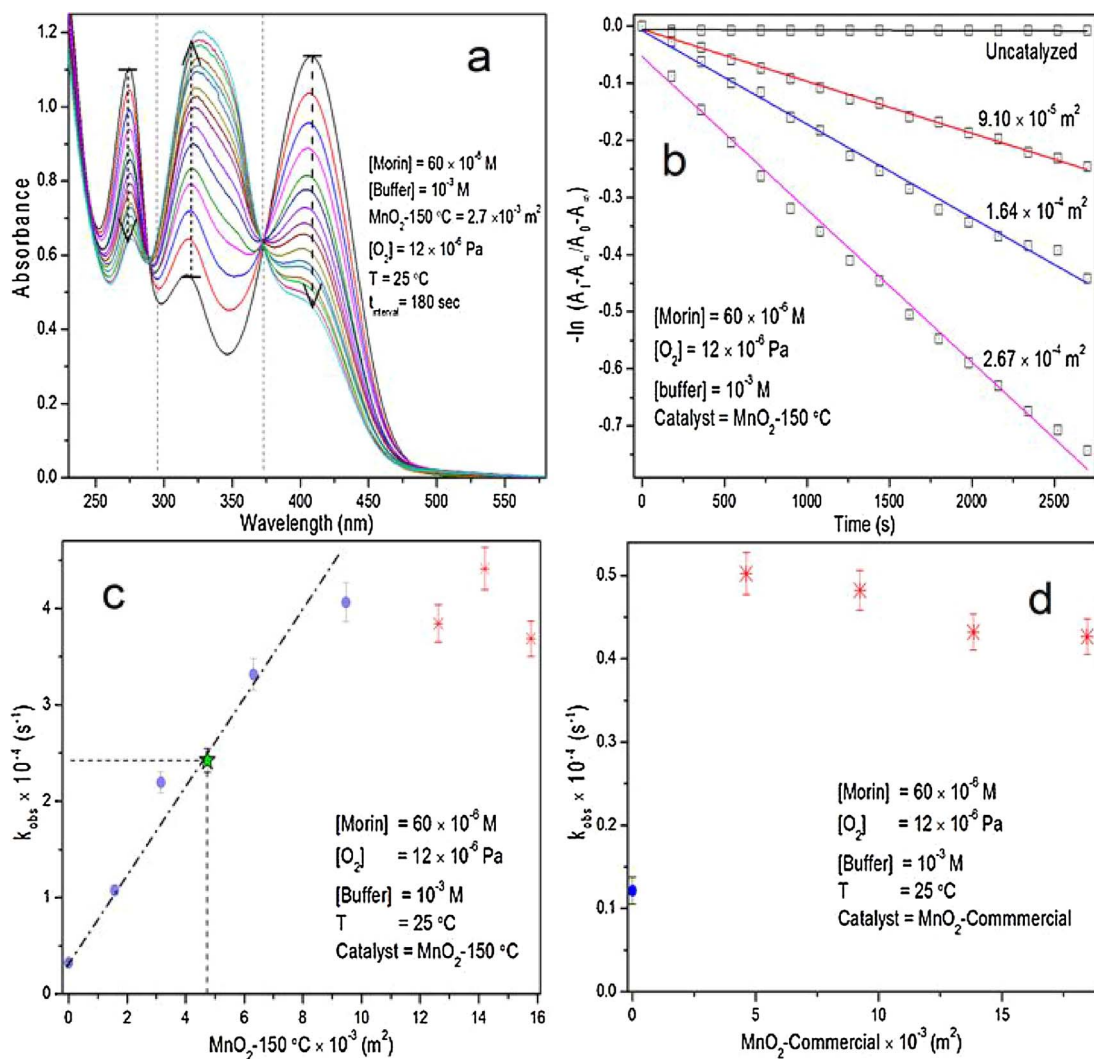
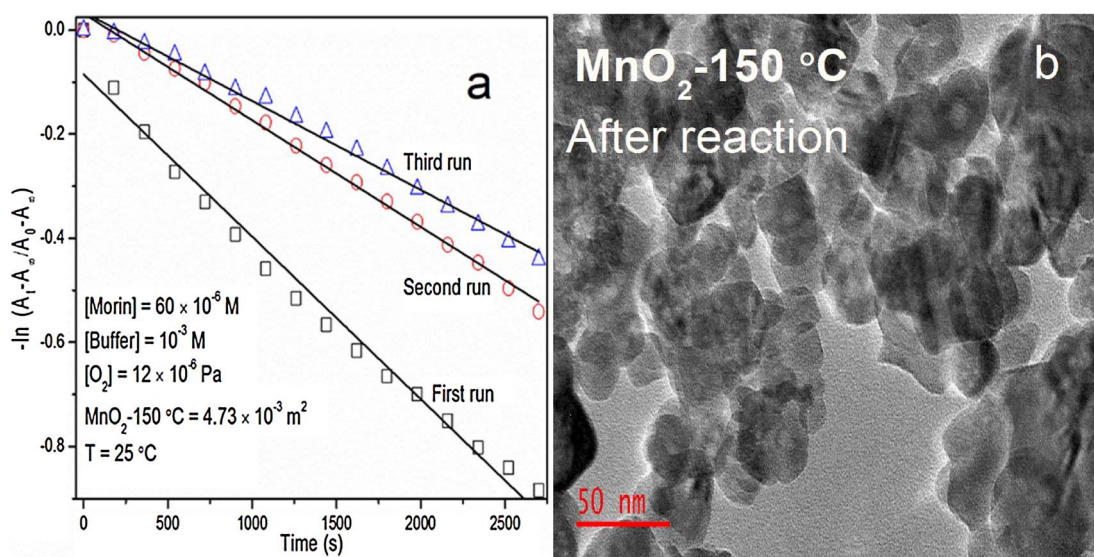


Fig. 5. Morin oxidation pathway.



**Fig. 6.** (a) shows the UV-vis spectra of aerobic oxidation of morin catalyzed by  $MnO_2-150^\circ\text{C}$ , (b) the kinetic pseudo-first order evaluation for the uncatalyzed and catalyzed ( $MnO_2-150^\circ\text{C}$ ) following at  $\lambda = 410 \text{ nm}$ , and the catalytic investigation using  $MnO_2-150^\circ\text{C}$  (c) and  $MnO_2$ -Commercial (d).



**Fig. 7.** Catalyst reusability investigated through recycle run (a) and micrograph capture after the last recycling run (b).

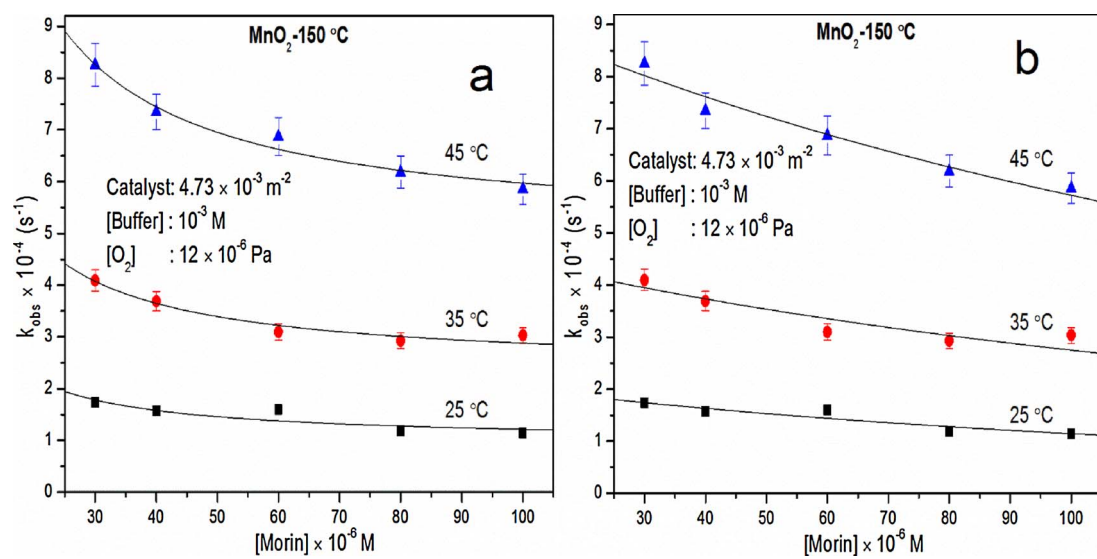


Fig. 8. Best fitted experimental data according to the Mars-van Krevelen ( $R^2 = 0.99$ ) (a) and Langmuir-Hinshelwood ( $R^2 = 0.97$ ) (b) approaches using  $\text{MnO}_2$ -150 °C as a catalyst, respectively.

nature of isothermal adsorption [33].

Without supplying air, the aerobic oxidation was conducted to investigate the oxidative ability of lattice oxygen. Before conducting the investigation, any potential oxygen gas adsorbed onto the catalyst interface was removed through a vacuum and the catalyst was kept under nitrogen gas. A solution of morin ( $60 \times 10^{-6}$  M) in  $20 \times 10^{-3}$  L of deionized water was kept under nitrogen gas for 30 min. Exactly,  $4.73 \times 10^{-3}$  m $^2$  of  $\text{MnO}_2$ -150 °C was added to oxidize morin without supplying the oxygen gas. The resulting spectra are shown in the supplementary information (Fig. 2S). The observed rate constant of the oxidation process was equaled to  $5.9 \times 10^{-5}$  s $^{-1}$  which prove the oxidative activity of the lattice oxygen in manganese oxide.

The kinetic and thermodynamic parameters of the interfacial interaction between catalyst and substrates were investigated using the highlighted green star in Fig. 6c and Fig. 1S as the surface area of mesoporous manganese oxide materials. At different temperatures, only the morin interfacial interaction was evaluated because the oxygen gas was continuously pumped at a fixed flow rate. The experimental data were fitted using the Mars-van Krevelen and Langmuir-Hinshelwood equations given in Eqs. (2a) and (2b), respectively. The best-fitting data for  $\text{MnO}_2$ -150 °C is depicted in Fig. 8a and b according to the Mars-van Krevelen and Langmuir-Hinshelwood equations, respectively. For the

rest of the mesoporous manganese oxide materials, the best-fitting data are shown in the supplementary information (Mars-van Krevelen approach (Fig. 3S), and Langmuir-Hinshelwood approach (Fig. 4S)). The assumption of aerobic oxidation of morin under oxygen gas catalyzed by mesoporous manganese oxide material is illustrated in Fig. 9. The resulting kinetic and thermodynamic parameters of the interfacial interaction between catalyst and substrate from the fitted experimental data are given in Table 3.

The dependence of the kinetic rate and equilibrium constants on temperature was investigated to determine the activation energy and the thermodynamic parameters (enthalpy and entropy of the activation). The activation energy of the aerobic oxidation was calculated using the Arrhenius equation [34]. The Arrhenius equation was constructed using kinetic rate constant on the catalyst surface versus the temperature. The thermodynamic parameters such as enthalpy and entropy of activation on the catalyst surface were calculated using the Eyring equation [35]. The interaction between the catalyst and substrate resulted in the equilibrium constant which was investigated using the Van't Hoff equation [36]. For all the catalysts, the Gibbs free activation energy was calculated at 25 °C using  $60 \times 10^{-6}$  M of morin. The activation energy and thermodynamic parameters are given in Table 4 for both adsorption isotherm approaches.

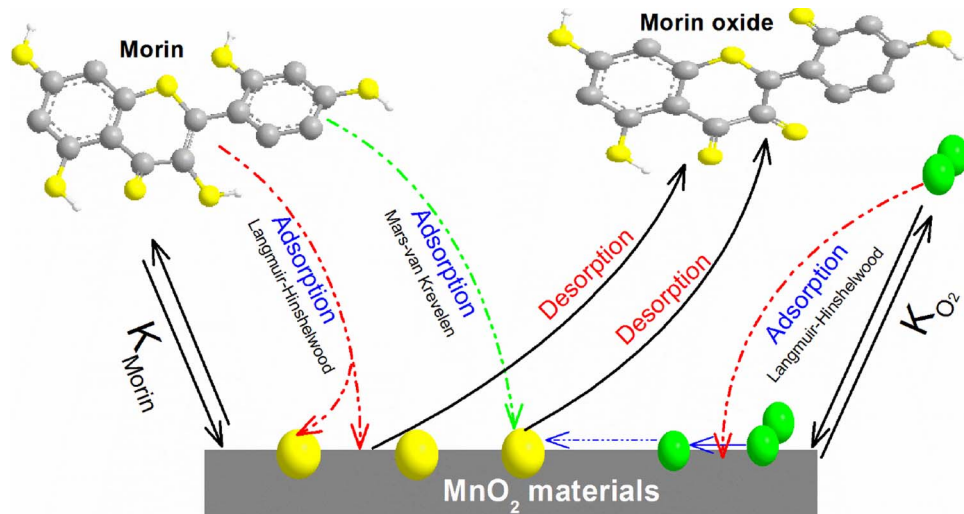


Fig. 9. Langmuir-Hinshelwood and Mars-van Krevelen approaches detailing the adsorption isotherm of morin and oxygen gas onto the mesoporous manganese oxide materials surface.

**Table 3**

The kinetic rate constant onto catalyst surface and equilibrium constant of the aerobic oxidation of morin.

Langmuir-Hinshelwood approach						
Catalyst	T (°C)	Parameters				
		$k_1$ (mol m <sup>-2</sup> s <sup>-1</sup> )	$K_{\text{Morin}} \times 10^{-2}$ (L mol <sup>-1</sup> )	$K_{\text{O}_2}$ (L mol <sup>-1</sup> )	n	m
$\text{MnO}_2$ -150 °C	25	102.2 ± 33.8	3.7 ± 1.1	9.1 ± 2.6	1.0 ± 0.0	0.9 ± 0.1
	35	124.2 ± 19.2	6.1 ± 2.3	18.8 ± 7.1	1.0 ± 0.0	1.0 ± 0.0
	45	150.4 ± 20.6	16.6 ± 8.0	58.6 ± 13.2	1.0 ± 0.0	0.9 ± 0.0
$\text{MnO}_2$ -250 °C	25	53.2 ± 11.3	0.7 ± 0.1	0.6 ± 0.2	1.0 ± 0.0	0.9 ± 0.1
	35	137.2 ± 42.4	1.3 ± 0.1	4.8 ± 1.8	1.0 ± 0.1	1.0 ± 0.0
	45	175.8 ± 52.3	8.3 ± 3.5	20.7 ± 13.4	1.0 ± 0.0	1.0 ± 0.1
$\text{MnO}_2$ -350 °C	25	12.9 ± 3.8	1.3 ± 0.4	1.8 ± 0.9	1.0 ± 0.1	0.9 ± 0.1
	35	22.1 ± 9.1	21.4 ± 5.2	65.6 ± 28.7	1.0 ± 0.0	0.9 ± 0.0
	45	111.4 ± 34.9	77.4 ± 13.6	256.9 ± 95.2	1.0 ± 0.1	0.9 ± 0.1
$\text{MnO}_2$ -450 °C	25	123.3 ± 18.9	1.2 ± 0.3	6.6 ± 2.3	1.0 ± 0.0	1.0 ± 0.0
	35	471.3 ± 145.3	2.2 ± 1.0	18.6 ± 4.9	1.0 ± 0.0	1.0 ± 0.1
	45	767.9 ± 238.3	2.4 ± 0.8	19.5 ± 5.5	1.0 ± 0.0	1.0 ± 0.0
$\text{MnO}_2$ -550 °C	25	155.8 ± 48.8	0.5 ± 0.0	1.1 ± 0.7	1.0 ± 0.1	1.0 ± 0.2
	35	645.8 ± 201.4	1.0 ± 0.3	9.8 ± 3.3	1.0 ± 0.0	1.0 ± 0.0
	45	1122.5 ± 335.9	7.2 ± 3.2	116.8 ± 68.1	1.0 ± 0.0	0.9 ± 0.1
Mars-van Krevelen approach						
Catalyst	T (°C)	Parameters				
		$k_1$ (mol m <sup>-2</sup> s <sup>-1</sup> )	$k_2 \times 10^{-4}$ (mol m <sup>-2</sup> s <sup>-1</sup> )	$k_3 \times 10^{-4}$ (mol m <sup>-2</sup> s <sup>-1</sup> )	n	m
$\text{MnO}_2$ -150 °C	25	0.2 ± 0.1	1.9 ± 0.2	1.9 ± 0.2	1.0 ± 0.1	1.0 ± 0.0
	35	0.3 ± 0.2	2.2 ± 1.6	2.2 ± 1.6	1.0 ± 0.0	1.0 ± 0.1
	45	0.4 ± 0.1	2.4 ± 0.9	2.4 ± 0.9	1.0 ± 0.0	1.0 ± 0.1
$\text{MnO}_2$ -250 °C	25	0.9 ± 0.5	1.3 ± 0.5	1.3 ± 0.5	1.0 ± 0.2	1.0 ± 0.3
	35	1.1 ± 0.5	2.4 ± 0.9	2.4 ± 0.9	1.0 ± 0.1	1.0 ± 0.1
	45	2.9 ± 1.4	2.0 ± 1.0	2.0 ± 1.0	1.0 ± 0.0	1.0 ± 0.0
$\text{MnO}_2$ -350 °C	25	0.2 ± 0.1	1.5 ± 0.9	1.5 ± 0.9	1.0 ± 0.1	1.0 ± 0.2
	35	0.5 ± 0.2	1.9 ± 1.0	1.9 ± 1.0	1.0 ± 0.0	1.0 ± 0.1
	45	1.3 ± 0.6	4.0 ± 1.8	4.0 ± 1.8	1.0 ± 0.1	1.0 ± 0.1
$\text{MnO}_2$ -450 °C	25	0.5 ± 0.3	2.0 ± 1.3	2.0 ± 1.3	1.0 ± 0.0	1.0 ± 0.0
	35	1.3 ± 0.6	3.4 ± 0.8	3.4 ± 0.8	1.0 ± 0.0	1.0 ± 0.2
	45	2.2 ± 1.0	5.3 ± 1.8	5.3 ± 1.8	1.0 ± 0.2	1.0 ± 0.1
$\text{MnO}_2$ -550 °C	25	0.9 ± 0.4	0.7 ± 0.3	0.7 ± 0.3	1.0 ± 0.1	1.0 ± 0.0
	35	1.4 ± 0.6	1.7 ± 0.9	1.7 ± 0.9	1.0 ± 0.1	1.0 ± 0.1
	45	2.1 ± 0.9	2.0 ± 1.3	2.0 ± 1.3	1.0 ± 0.0	1.0 ± 0.0

The nature of the active sites on the catalyst interface as defined by the Langmuir-Hinshelwood approach is unspecified. The resulting catalytic activity of the interfacial interaction engaging the catalyst and substrate is attributed to the unspecified active site on the catalyst interface [30]. The Mars-van Krevelen approach attributed the catalytic activity resulting from the interfacial interaction between catalyst and substrate to the lattice oxygen [26]. To calculate the activity on the interface of the mesoporous manganese oxide materials, the Arrhenius-type plot was constructed using the normalized kinetic rate constant ( $k_1$  and  $k_2$ ) to the surface area (green star) [37,38]. Both physicochemical adsorption approaches can be applied in our investigation, therefore we can isolate the individual activity on the catalyst surface for the metal, the lattice oxygen, and the oxygen gas [39–42]. By subtracting the activities of the catalyst surface from the Langmuir-Hinshelwood approach to the ones from the Mars-van Krevelen approach we can effectively determine the activity related to the metal or manganese. The activity of the catalyst surface is given in Table 5 and Fig. 10a illustrates the activity magnitude of the lattice oxide and manganese.

The incorporation of lattice oxygen to the adsorbed substrate resulted in an electronic state change of the catalyst oxo-cluster structure. The electronic state of the metal oxide is restored by reoxidizing of the catalyst with the oxygen gas [26]. Applying the Arrhenius-type

equation, the activity of oxygen gas was determined for all the mesoporous manganese oxide materials. The Arrhenius-type plot was constructed using the normalized kinetic rate constant ( $k_2$ ) to the catalyst surface area versus the temperature. The activity of the oxygen gas is given in Table 5 and Fig. 10b shows the magnitude of the activity between the oxygen gas and the lattice oxygen.

#### 4. Discussion

The nitrogen gas adsorption isotherm plots indicate the Type-IV hysteresis loops assigned by Brunauer (Fig. 1a) [43]. The Type-IV adsorption isotherm was observed for all the manganese oxide materials proving the regularity of mesoporous and monomodal pore structures [16]. The pore size distributions for all the mesoporous manganese oxide materials indicated a large value compared to the ones reported in the literature (Fig. 1b) [44]. The mesoporous structure and large pore size of the mesoporous manganese oxide materials showed the possibility of interfacial interaction between the catalyst and substrates. The heat treatment fundamentally impacted on the mesoporous manganese oxide materials tunable properties. The surface area increases along with the heat treatment temperature, however, the opposite is indicated for the pore size. BET analysis results are given in Table 1 for all the

Table 4

The activation energy and thermodynamic parameters of morin oxidation using mesoporous manganese oxide materials as catalysts.

Langmuir-Hinshelwood					
Catalyst	Parameters	$E_a$ (kJ mol <sup>-1</sup> )	$\Delta H^\#$ (kJ mol <sup>-1</sup> )	$\Delta S^\#$ (J mol <sup>-1</sup> )	$\Delta G^{\#(a)}$ (kJ mol <sup>-1</sup> )
$MnO_2$ -150 °C	$k_{obs}$ (mol m <sup>-2</sup> s)	57.8 ± 4.1	55.1 ± 4.1	250.1 ± 19.9	-19.5
	$k_1$ (mol m <sup>-2</sup> s)	15.2 ± 2.5	61.6 ± 2.6	367.0 ± 19.0	-47.8
	$K_{Morin}$ (L mol <sup>-1</sup> )	-	62.3 ± 11.5	180.8 ± 36.9	8.5
	$K_{O_2}$ (L mol <sup>-1</sup> )	-	69.5 ± 10.6	251.3 ± 34.7	-5.4
$MnO_2$ -250 °C	$k_{obs}$ (mol m <sup>-2</sup> s)	58.0 ± 13.4	54.7 ± 13.6	256.1 ± 29.7	-21.6
	$k_1$ (mol m <sup>-2</sup> s)	47.3 ± 1.1	19.3 ± 1.2	241.4 ± 19.5	-52.7
	$K_{Morin}$ (L mol <sup>-1</sup> )	-	107.1 ± 24.5	315.6 ± 78.4	13.1
	$K_{O_2}$ (L mol <sup>-1</sup> )	-	145.9 ± 9.4	485.9 ± 31.4	1.1
$MnO_2$ -350 °C	$k_{obs}$ (mol m <sup>-2</sup> s)	91.2 ± 17.3	87.4 ± 17.4	356.6 ± 24.4	-18.8
	$k_1$ (mol m <sup>-2</sup> s)	73.8 ± 27.3	92.2 ± 22.1	466.7 ± 26.0	-46.8
	$K_{Morin}$ (L mol <sup>-1</sup> )	-	124.3 ± 26.9	388.9 ± 84.8	8.4
	$K_{O_2}$ (L mol <sup>-1</sup> )	-	219.8 ± 37.1	742.5 ± 14.3	-1.5
$MnO_2$ -450 °C	$k_{obs}$ (mol m <sup>-2</sup> s)	64.9 ± 13.6	63.3 ± 13.5	284.7 ± 29.5	-21.5
	$k_1$ (mol m <sup>-2</sup> s)	75.3 ± 16.9	70.2 ± 25.8	416.0 ± 26.6	-53.8
	$K_{Morin}$ (L mol <sup>-1</sup> )	-	27.6 ± 12.7	56.6 ± 15.0	10.7
	$K_{O_2}$ (L mol <sup>-1</sup> )	-	46.9 ± 18.7	173.9 ± 61.3	-4.9
$MnO_2$ -550 °C	$k_{obs}$ (mol m <sup>-2</sup> s)	68.4 ± 11.1	66.6 ± 11.1	289.9 ± 22.6	-19.8
	$k_1$ (mol m <sup>-2</sup> s)	81.2 ± 17.2	84.4 ± 19.7	464.2 ± 25.6	-53.9
	$K_{Morin}$ (L mol <sup>-1</sup> )	-	112.8 ± 26.9	332.1 ± 86.3	13.8
	$K_{O_2}$ (L mol <sup>-1</sup> )	-	172.8 ± 8.9	581.1 ± 30.1	-0.3
$Mn_xNP@SPB$	$kS$ (mol m <sup>-2</sup> L <sup>-1</sup> s <sup>-1</sup> )	45.8 ± 7.0	-	-	Ref.: [22]
	$K_{Morin}$ (L mol <sup>-1</sup> )	-	-19.8 ± 8.7	0.2 ± 29.6	
	$K_{H_2O_2}$ (L mol <sup>-1</sup> )	-	-20.8 ± 3.1	-26.1 ± 10.7	
Mars-van Krevelen					
Catalyst	Parameters	$E_a$ (kJ mol <sup>-1</sup> )	$\Delta H^\#$ (kJ mol <sup>-1</sup> )	$\Delta S^\#$ (J mol <sup>-1</sup> )	$\Delta G^{\#(a)}$ (kJ mol <sup>-1</sup> )
$MnO_2$ -150 °C	$k_1$ (mol m <sup>-2</sup> s)	14.9 ± 0.9	52.3 ± 1.1	302.7 ± 19.2	-37.9
	$k_2$ (mol m <sup>-2</sup> s)	9.4 ± 1.1	6.8 ± 1.1	90.1 ± 38.5	-20.0
	$k_3$ (mol m <sup>-2</sup> s)	9.4 ± 1.1	6.8 ± 1.1	90.1 ± 38.5	-20.0
$MnO_2$ -250 °C	$k_1$ (mol m <sup>-2</sup> s)	19.8 ± 8.1	45.3 ± 16.2	288.4 ± 38.1	-40.6
	$k_2$ (mol m <sup>-2</sup> s)	18.2 ± 9.4	15.9 ± 7.2	118.1 ± 41.6	-19.3
	$k_3$ (mol m <sup>-2</sup> s)	18.2 ± 9.4	15.9 ± 7.2	118.1 ± 41.6	-19.3
$MnO_2$ -350 °C	$k_1$ (mol m <sup>-2</sup> s)	69.2 ± 5.4	62.5 ± 5.5	336.2 ± 23.6	-37.7
	$k_2$ (mol m <sup>-2</sup> s)	38.4 ± 12.1	35.5 ± 12.2	183.6 ± 71.0	-19.2
	$k_3$ (mol m <sup>-2</sup> s)	38.4 ± 12.1	35.5 ± 12.2	183.6 ± 71.0	-19.2
$MnO_2$ -450 °C	$k_1$ (mol m <sup>-2</sup> s)	57.0 ± 9.4	51.1 ± 6.5	305.3 ± 2.9	-39.9
	$k_2$ (mol m <sup>-2</sup> s)	38.0 ± 1.1	35.5 ± 12.2	183.6 ± 80.4	-19.2
	$k_3$ (mol m <sup>-2</sup> s)	38.0 ± 1.1	35.5 ± 12.2	183.6 ± 80.4	-19.3
$MnO_2$ -550 °C	$k_1$ (mol m <sup>-2</sup> s)	34.9 ± 0.2	32.6 ± 0.2	246.7 ± 18.5	-40.9
	$k_2$ (mol m <sup>-2</sup> s)	40.1 ± 15.9	37.9 ± 15.8	187.4 ± 85.0	-17.9
	$k_3$ (mol m <sup>-2</sup> s)	40.1 ± 15.9	37.9 ± 15.8	187.4 ± 85.0	-17.9

Table 5

Activity of the metal, lattice oxygen, and oxygen gas.

Catalysts	Activity × (kJ mol <sup>-1</sup> m <sup>-2</sup> )		
	Metal (manganese)	Lattice Oxygen	Oxygen gas
$MnO_2$ -150 °C	0.3 ± 0.1	14.9 ± 0.2	9.4 ± 1.1
$MnO_2$ -250 °C	1.4 ± 0.8	45.9 ± 16.9	18.7 ± 9.4
$MnO_2$ -350 °C	20.1 ± 9.7	64.3 ± 5.6	37.6 ± 12.3
$MnO_2$ -450 °C	17.8 ± 7.8	54.5 ± 6.4	14.6 ± 8.1
$MnO_2$ -550 °C	42.9 ± 18.0	35.2 ± 0.3	41.1 ± 14.5

mesoporous materials including the commercial manganese oxide.

The XRD plots showed a couple of diffracting peaks assessing the crystallinity of the mesoporous manganese oxide materials (Fig. 2(a–b)). All the manganese oxide materials matched to the manganese oxide crystallinity which was confirmed by the JSCD numbers. The matched JSCD numbers shifted from  $MnO$  (96-900-3477) for  $MnO_2$ -(150–250 °C) to  $MnO_2$  (96-441-7967) for  $MnO_2$ -(250–550 °C).

The crystallite size of the mesoporous manganese oxide materials increased proportionally to the heat treatment temperature. The crystallite size of the mesoporous materials is given in Table 1. The large value of the calculated crystallite size of the mesoporous manganese oxide materials explained the observed lower value of the surface area [45].

The micrograph was captured at two magnitudes to visualize the shape and interface structure of the mesoporous manganese oxide materials. The lower-magnitude micrograph (20 nm) shows the meso-channel frameworks of the mesoporous manganese oxide materials. That confirmed the mesopore structure regularity of the mesoporous manganese oxide materials [10]. The higher-magnitude micrograph (50 nm) shows a diverse crystallite shape of the mesoporous manganese oxide materials. The varied shape demonstrates the structure softness of the mesoporous manganese oxide materials. The micrographs of the mesoporous manganese oxide materials are depicted in Fig. 3(a–e).

TPR analysis indicated a couple of reduction peaks assessing the reducibility of the mesoporous manganese oxide materials [46]. A couple of reduction peaks shows the multiple oxidation states of the mesoporous manganese oxide materials [47]. Fig. 4 depicted the

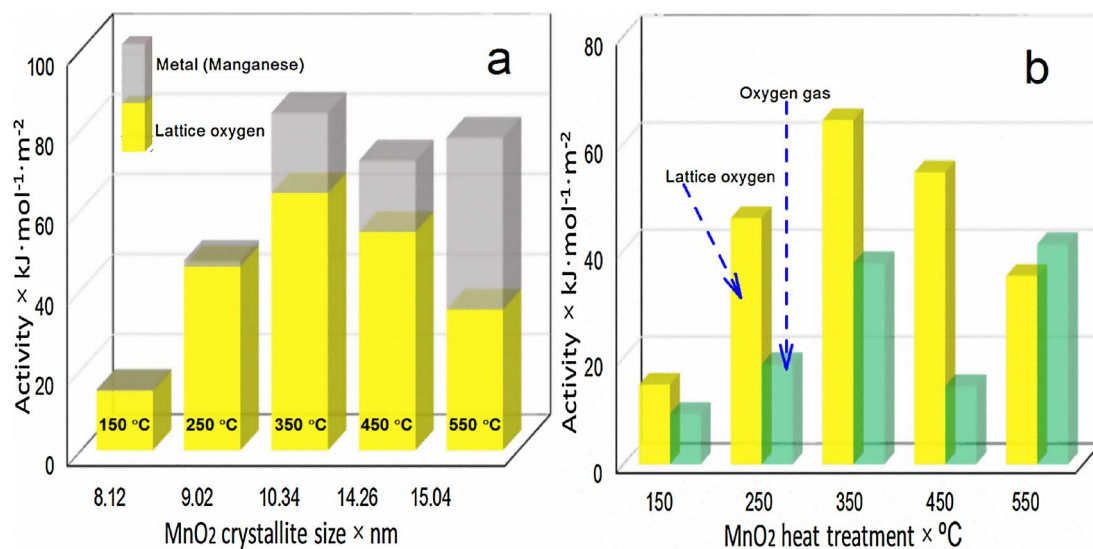


Fig. 10. Activity of the lattice oxygen and metal (manganese) (a) and activity of lattice oxygen and oxygen gas (b).

reduction peak of the mesoporous manganese oxide materials.  $\text{MnO}_2$ –150 °C and  $\text{MnO}_2$ –250 °C show two reduction peaks ( $\text{MnO}_2$  to  $\text{Mn}_2\text{O}_3$  and  $\text{Mn}_2\text{O}_3$  to  $\text{Mn}_3\text{O}_4$ ).  $\text{MnO}_2$ –350 °C,  $\text{MnO}_2$ –450 °C, and  $\text{MnO}_2$ –550 °C show three reduction peaks ( $\text{MnO}_2$  to  $\text{Mn}_2\text{O}_3$ ,  $\text{Mn}_2\text{O}_3$  to  $\text{Mn}_3\text{O}_4$ , and  $\text{Mn}_3\text{O}_4$  to  $\text{MnO}$ ). The reduction peaks corresponded to the stepwise reduction of the manganese oxide reported by Stobbe [45]. The multiple oxidation states of the mesoporous manganese oxide materials support its oxidative activity in the oxidation process [47,48]. The temperature corresponding to the reduction peaks of the mesoporous manganese oxide materials is shown in Table 2.

The oxidation of morin led to the formation of two benzoic acids, however, the oxidation pathway is not precisely known [22]. One of the highly probable mechanism pathways of morin oxidation can be the formation of morin oxide as the first step [21,22]. Recently, we performed a liquid chromatography analysis of morin oxidation which confirmed the formation of morin oxide as an intermediate [49]. The mechanism of morin oxidation is schematized in Fig. 5. Through UV–vis spectrophotometry, the adsorption spectrum decreased over time at  $\lambda$  410 nm, which wavelength was followed to monitor the aerobic oxidation of morin (Fig. 6a). The kinetics of morin oxidation conducted under *pseudo*-first order conditions is depicted in Fig. 6b. The morin concentration decrease linearly with the time, which confirms the *pseudo*-first order conditions [29].

The uncatalyzed aerobic oxidation of morin resulted in a significantly lower reaction rate than the catalyzed reaction. The reaction rate increases linearly along with the mesoporous manganese oxide materials. This shows the catalytic activity of the mesoporous manganese oxide materials. The catalyst effect investigation is depicted in Fig. 6c and Fig. 1S. The linear increase of the reaction rate defines the kinetic zone and the horizontal development of the reaction rate indicates the mass transport limitation [50]. The kinetic investigation was performed using the catalyst amount located in the kinetic domain illustrated as a green star in Fig. 6c and Fig. 1S. The reaction rate horizontally increases in the presence of commercial manganese oxide materials (Fig. 6d). That indicates the inactivity of the commercial manganese oxide.

Three recycling runs were performed to analyze the reusability of the mesoporous manganese oxide materials.  $\text{MnO}_2$ –150 °C, surface area of  $4.73 \times 10^{-3} \text{ m}^2$ , was used to perform the recycling investigation and the catalyst recovery was performed by centrifugation. The observed rate constant declining through the recycling process can probably be caused by the catalyst sintering during the course of the recycling (Fig. 7a) [51]. The catalyst micrograph captured at 50 nm magnification after the last recycling run shows a similar image to the fresh

catalyst (Fig. 7b). The catalyst micrographs captured before and after the aerobic oxidation show a similar crystallite shape which suggests the catalyst stability during the oxidation process. The ICP-MS analysis indicated a low presence of manganese digested in water (0.16 ppm). That proves the stability in water of the mesoporous manganese oxide materials which support its reusability during the oxidation process.

The reaction rate of the aerobic oxidation without supplying air is four times lower compared to the air supplied process. The resulting activity can rely on the presence of lattice oxygen in mesoporous metal oxide material. The UV–vis spectra of oxidation process are shown in Fig. 2S. The low reaction rate can be understood by the lack of oxidation state restoration of mesoporous manganese oxide material. The aerobic oxidation of morin under oxygen gas certainty occurred following the Mars–van Krevelen approach [26]. The lattice oxygen in the mesoporous manganese oxide materials plays an effective role of an oxidant for the aerobic oxidation of morin.

The best-fitted curve using both adsorption isotherm approaches, Mars–van Krevelen and Langmuir–Hinshelwood indicated a good correlation between both models with the experimental data. Using  $\text{MnO}_2$ –150 °C as a catalyst, the best-fitting data shown in Fig. 8(a–b) gave an R-squared value close to unity for both approaches, Mars–van Krevelen (0.99) and Langmuir–Hinshelwood (0.97). The Sips exponential constants, n, and m, had a value close to unity which indicated the linearity of the isothermic adsorption of the substrate onto the catalyst surface [33].

The kinetic rate ( $k_1$ ,  $k_2$ , and  $k_3$ ) and equilibrium ( $K_{\text{morin}}$  and  $K_{\text{O}_2}$ ) constants increase along with the temperature for both isothermic adsorption approaches. Table 3 gives the kinetic rate and equilibrium constants for the isothermic adsorption approaches. The kinetic rate constant ( $k_1$ ) resulting from the interfacial interaction between substrate and catalyst is relatively defined by the applied adsorption approach. The Mars–van Krevelen approach referred the kinetic rate constant ( $k_1$ ) to the interfacial interaction between lattice oxygen and substrate [26]. The kinetic rate constant ( $k_1$ ) according to the Langmuir–Hinshelwood approach is referred to the interfacial interaction between active site and substrate [30]. The assumption of the interfacial interaction between substrate and catalyst was illustrated in Fig. 9.

The activation energy of the mesoporous manganese oxide materials calculated using the observed rate constant ( $k_{\text{obs}}$ ) showed a higher value compared to the one using the kinetic rate constants ( $k_1$  or  $k_2$ ). Except for  $\text{MnO}_2$ –(450 °C and 550 °C), the activation energy from  $k_1$  is higher than  $k_{\text{obs}}$  according to the Langmuir–Hinshelwood approach. This difference can be explained by the fact that the observed rate

constant included the kinetic rate and equilibrium constants [22]. Lattice oxygen has a higher activation energy than the oxygen gas (dissociation and incorporation). The role of the oxygen gas consisted of metal oxide electronic state recovery [26]. This demonstrated the capacity of the catalyst structure to be restored and its catalytic reusability. The identical value of the activation energy during the dissociation and incorporation of oxygen gas indicated a perfect interfacial interaction between the oxygen gas and the catalyst. The activation energy is given in Table 4 for both adsorption isotherm approaches.

Polzer et al. evaluated the catalytic activity of manganese oxide nanoparticles immobilized on cationic spherical polyelectrolyte brushes ( $Mn_xNP@SPB$ ) using morin oxidation by hydrogen peroxide as a model reaction [22]. The kinetic data were interpreted based on the Langmuir–Hinshelwood approach. The activation energy of the immobilized manganese oxide nanoparticles was  $(45.8 \pm 7.0) \text{ kJ mol}^{-1}$  which is a large value compared to this work's value according to the Mars–van Krevelen approach (Table 4). This demonstrated a great interfacial interaction between substrate and catalyst for the mesoporous manganese oxide compared to the immobilized manganese oxide nanoparticles.

Both adsorption processes indicated an endothermic interfacial interaction of substrate onto the catalyst as described by a positive value of the enthalpy of activation (Table 4). Morin oxidation catalyzed by metal transition nanoparticles adsorption process was similarly reported to be an endothermic interfacial interaction [30]. The entropy of activation showed a larger value for both adsorption isotherm approaches which might indicate the complexity of the interfacial interaction of substrates onto the catalyst. The substrates interfacial interaction onto the catalyst lattice oxygen consists of a spontaneous process based on the negative value of the Gibbs free activation energy. The Langmuir–Hinshelwood approach revealed a non-spontaneous process during the interfacial interaction of the substrate with the catalyst surface (Table 4).

The activity on the catalyst surface increases along with the catalyst crystallite size (Fig. 10a) which can suggest the improvement of interfacial interaction between the substrates and catalyst active sites.  $MnO_2$ –350 °C was found to be the optimum activity of the lattice oxygen and  $MnO_2$ –550 °C represents a relatively close value of the activity for both, metal and lattice oxygen (Table 5). From 350 °C of catalyst heat treatment, we observed a negligible change in the activity on the catalyst surface. However, we noticed an increase in the manganese activity. That can also suggest that an increase of heat treatment temperature does result in removal of lattice oxygen and increase the density of metal (manganese) [16].

The activity of the oxygen gas is equal to its dissociation. The activity of the oxygen gas increases proportionally to the catalyst heat treatment (Table 5).  $MnO_2$ –350 °C consists of the optimum temperature in the heat treatment of catalyst resulted in high activity of electronic state restoration (Fig. 10b). For most of the mesoporous manganese oxide materials, the electronic state restoration activity was found to be at lower value compared to the lattice oxygen activity, except for  $MnO_2$ –550 °C (Fig. 10b). We believed that the large activity of metal on  $MnO_2$ –550 °C could be the reason which may improve the oxygen gas adsorption and dissociation on the catalyst surface.

## 5. Conclusion

The surface area, porosity, crystallinity, and reducibility of the mesoporous manganese oxide materials were significantly modified by the heat treatment. The porosity and crystallinity were found to increase along with the increase of the heat treatment temperature. However, the surface area was found to decrease along with the increase of heat treatment temperature. The mesoporous manganese oxide materials demonstrated an effective catalytic activity for a complete aerobic oxidation of morin under oxygen gas. The experimental data interpreted according to the Mars–van Krevelen and Langmuir–Hinshelwood approaches fitted perfectly and led to the determination

of kinetic and thermodynamic parameters on the mesoporous manganese oxide materials interface. The Arrhenius-type plot allowed the determination of the activity of the manganese, lattice oxygen, and oxygen gas.  $MnO_2$ –350 °C exhibited the largest lattice oxygen activity where  $MnO_2$ –550 °C indicated the largest manganese activity.

## Acknowledgments

This work was supported by the National Research Foundation of South Africa {Grant specific unique reference number (UID) 5386}. We acknowledge the University of Johannesburg for funding as well as Mr. D. Harris and Dr. R. Meyer from Shimadzu South Africa for the use of their equipment.

## Appendix A. Supplementary data

Supplementary data associated with this article can be found, in the online version, at <http://dx.doi.org/10.1016/j.apcatb.2017.11.032>.

## References

- [1] C.T. Kresge, M.E. Leonowicz, W.J. Roth, J.C. Vartuli, J.S. Beck, *Nature* 359 (1992) 710–712.
- [2] S.H. Joo, J.Y. Park, C.-K. Tsung, Y. Yamada, P. Yang, G.A. Somorjai, *Nat. Mater.* 8 (2009) 126–131.
- [3] R. Demir-Cakan, Y.-S. Hu, M. Antonietti, J. Maier, M.-M. Titirici, *Chem. Mater.* 20 (2008) 1227–1229.
- [4] M. Vallet-Regi, F. Balas, D. Arcos, *Angew. Chem. Int. Ed.* 46 (2007) 7548–7558.
- [5] A. Taguchi, F. Schüth, *Microporous Mesoporous Mat.* 77 (2005) 1–45.
- [6] P. Yang, S. Gai, J. Lin, *Chem. Soc. Rev.* 41 (2012) 3679–3698.
- [7] R. Liu, S.B. Lee, *J. Am. Chem. Soc.* 130 (2008) 2942–2943.
- [8] T.-W. Kim, R. Ryoo, M. Kruk, K.P. Gierszal, M. Jaroniec, S. Kamiya, O. Terasaki, *J. Phys. Chem. B* 108 (2004) 11480–11489.
- [9] G.Z. Kyzas, K.A. Matis, *J. Mol. Liq.* 203 (2015) 159–168.
- [10] S. Biswas, A.S. Poyraz, Y. Meng, C.-H. Kuo, C. Guild, H. Tripp, S.L. Suib, *Appl. Catal. B Environ.* 165 (2015) 731–741.
- [11] S. Choi, I.E. Wachs, *ACS Pet. Chem. Prepr.* 47/1 (2002) 137–138.
- [12] Y. Ren, Z. Ma, P.G. Bruce, *Chem. Soc. Rev.* 41 (2012) 4909–4927.
- [13] D. Gu, F. Schüth, *Chem. Soc. Rev.* 43 (2014) 313–344.
- [14] F. Schüth, *Chem. Mater.* 13 (2001) 3184–3195.
- [15] B. Tian, X. Liu, B. Tu, C. Yu, J. Fan, L. Wang, S. Xie, G.D. Stucky, D. Zhao, *Nat. Mater.* 2 (2003) 159–163.
- [16] A.S. Poyraz, C.-H. Kuo, S. Biswas, C.K. King'ondu, S.L. Suib, *Nat. Commun.* 4 (2013) 2952.
- [17] F. Garin, *Appl. Catal. A Gen.* 222 (2001) 183–219.
- [18] V.K. Gupta, S. Khamparia, I. Tyagi, D. Jaspal, A. Malviya, *Glob. J. Environ. Sci. Manag. Glob. J. Environ. Sci. Manag.* 1 (2015) 71–94.
- [19] Z. hua Liu, Y. Kanjo, S. Mizutani, *Sci. Total Environ.* 407 (2009) 731–748.
- [20] J.J. Dannacher, *J. Mol. Catal. A Chem.* 251 (2006) 159–176.
- [21] S. Rothbart, E. Ember, R. van Eldik, *Dalton Trans.* 39 (2010) 3264–3272.
- [22] F. Polzer, S. Wunder, Y. Lu, M. Ballauff, *J. Catal.* 289 (2012) 80–87.
- [23] A. Osman, D.P. Makris, P. Kefalas, *Process Biochem.* 43 (2008) 861–867.
- [24] I.G. Zenkevich, A.Y. Eshchenko, S.V. Makarova, A.G. Vitenberg, Y.G. Dobryakov, V.A. Utsal, *Molecules* 12 (2007) 654–672.
- [25] K.Y. Foo, B.H. Hameed, *Chem. Eng. J.* 156 (2010) 2–10.
- [26] I.E. Wachs, *Catal. Today* 100 (2005) 79–94.
- [27] Q. Wang, S.R. Kanel, H. Park, A. Ryu, H. Choi, *J. Nanoparticle Res.* 11 (2009) 749–755.
- [28] P. Yang, D. Zhao, D.I. Margolese, B.F. Chmelka, G.D. Stucky, *Nature* 396 (1998) 152–155.
- [29] Y.C. Wong, Y.S. Szeto, W.H. Cheung, G. McKay, *J. Appl. Polym. Sci.* 92 (2004) 1633–1645.
- [30] S. Alayoglu, K. An, G. Melaet, S. Chen, F. Bernardi, L.W. Wang, A.E. Lindeman, N. Musselwhite, J. Guo, Z. Liu, M.A. Marcus, G.A. Somorjai, *J. Phys. Chem. C* 117 (2013) 26608–26616.
- [31] A.K. Ilunga, R. Meijboom, *J. Mol. Catal. A Chem.* 411 (2016) 48–60.
- [32] N.C. Antonels, R. Meijboom, *Langmuir* 29 (2013) 13433–13442.
- [33] C. Rill, Z.I. Kolar, G. Kickelbick, H.T. Wolterbeek, J.A. Peters, *Langmuir* 25 (2009) 2294–2301.
- [34] J.M. Hunt, M.D. Lewan, R.J.C. Hennet, *Am. Assoc. Pet. Geol. Bull.* 75 (1991) 795–807.
- [35] J.J. Rooney, *J. Mol. Catal. A Chem.* 129 (1998) 131–134.
- [36] W.-Y. Chen, H.-M. Huang, C.-C. Lin, F.-Y. Lin, Y.-C. Chan, *Langmuir* 19 (2003) 9395–9403.
- [37] M.A. Vannice, *J. Mol. Catal.* 59 (1990) 165–177.
- [38] S.D. Lin, M.A. Vannice, *J. Catal.* 143 (1993) 539–553.
- [39] A.-P. Jia, S.-Y. Jiang, J.-Q. Lu, M.-F. Luo, *J. Phys. Chem. C* 114 (2010) 21605–21610.
- [40] M. Ilyas, M. Sadiq, *Chem. Eng. Technol.* 30 (2007) 1391–1397.

[41] S. Mohammad, I. Mohammad, Chin. J. Chem. 28 (2010) 2216–2220.

[42] P. Hurtado, S. Ordóñez, H. Sastre, F.V. Diez, Appl. Catal. B Environ. 51 (2004) 229–238.

[43] J. Lu, P. Zhang, A. Li, F. Su, T. Wang, Y. Liu, J. Gong, Chem. Commun. 49 (2013) 5817–5819.

[44] N.D. Wasalathantri, A.S. Poyraz, S. Biswas, Y. Meng, C.-H. Kuo, D.A. Kriz, S.L. Suib, J. Phys. Chem. C 119 (2015) 1473–1482.

[45] E.R. Stobbe, B.A. de Boer, J.W. Geus, Catal. Today 47 (1999) 161–167.

[46] V. Idakiev, T. Tabakova, K. Tenchev, Z.-Y. Yuan, T.-Z. Ren, B.-L. Su, J. Porous Mater. 19 (2012) 15–20.

[47] A. Iyer, J. Del-Pilar, C.K. King'ondu, E. Kissel, H.F. Garces, H. Huang, A.M. El-Sawy, P.K. Dutta, S.L. Suib, J. Phys. Chem. C 116 (2012) 6474–6483.

[48] L. Zhang, Y. Nie, C. Hu, X. Hu, J. Hazard. Mater. 190 (2011) 780–785.

[49] A.K. Ilunga, R. Meijboom, Appl. Catal. A Gen. 509 (2016) 17–29.

[50] P. Hervés, M. Pérez-Lorenzo, L.M. Liz-Marzán, J. Dzubiella, Y. Lu, M. Ballauff, Chem. Soc. Rev. 41 (2012) 5577–5587.

[51] J. Barbero, M.A. Peña, J.M. Campos-Martín, J.L.G. Fierro, P.L. Arias, Catal. Lett. 87 (2003) 211–218.